

ATOMIC-RESOLUTION Z-CONTRAST IMAGING AND ITS APPLICATION TO COMPOSITIONAL ORDERING AND SEGREGATION

S. J. PENNYCOOK^{a,b}, Y. YAN^c, A. NORMAN^c, Y. ZHANG^c, M. AL-JASSIM^c, A. MASCARENHAS^c, S.P. AHRENKIEL^c, M. F. CHISHOLM^a, G. DUSCHER^{a,b} and S. T. PANTELIDES^{a,b}

^a Solid State Division, Oak Ridge National Laboratory, Oak Ridge, Tennessee 37831-6030

^b Department of Physics and Astronomy, Vanderbilt University, Nashville TN 37235, USA

^c National Renewable Energy Laboratory, 1617 Cole Boulevard, Golden, Colorado 80401

INTRODUCTION

In the last ten years, the scanning transmission electron microscope (STEM) has become capable of forming electron probes of atomic dimensions making possible a new approach to high-resolution electron microscopy, Z-contrast imaging. Formed by mapping the intensity of high-angle scattered electrons as the probe is scanned across the specimen, the Z-contrast image represents a direct map of the specimen scattering power at atomic resolution. It is an incoherent image, and can be directly interpreted in terms of atomic columns. High angle scattering comes predominantly from the atomic nuclei, so the scattering cross section depends on atomic number (Z) squared. Z-contrast microscopy can therefore be used to study compositional ordering and segregation at the atomic scale. Here we present three examples of ordering: first, ferroelectric materials, second, III-V semiconductor alloys, and finally, cooperative segregation at a semiconductor grain boundary, where a combination of Z-contrast imaging with first principles theory provides a complete atomic-scale view of the sites and configurations of the segregant atoms.

DIRECT IMAGING WITH ELECTRONS

The images we see with our eyes generally appear to be a direct representation of the world around us. This is because they are *incoherent* images; objects are illuminated by light over a large range of directions and the intensity scattered depends primarily on the nature of the object and not on the direction of illumination. If objects are illuminated by coherent laser light they show a speckle pattern, which is due to interference effects. These are directly related to the object, but not in a manner that can be directly interpreted. Except for special applications, optical instruments such as a projector or a microscope invariably use incoherent illumination to maintain this capability for direct interpretation.

It is over one hundred years since Lord Rayleigh first explained the difference between coherent and incoherent imaging in the context of the light microscope¹. He clearly pointed out the advantages of incoherent imaging: absence from interference artifacts, and in addition a factor of two improved resolution. Ideally, a self-luminous object is required for perfect incoherent imaging, so that each point will emit light independently. But Lord Rayleigh showed how the condenser lens can be used to give a close approximation to incoherent imaging. If the condenser lens subtends a sufficiently large range of angles, then we approach the incoherent imaging conditions of normal vision.

It is now possible to achieve incoherent images of materials at atomic resolution with the scanning transmission electron microscope (STEM), shown schematically in Fig. 1. A small electron probe is scanned across a thin specimen, and a Z-contrast image results from mapping the intensity of electrons reaching the high angle annular detector². By enforcing high scattering angles, the image is dominated by Rutherford scattering from the nuclei, so that atoms contribute to the image with a brightness determined by their mean square atomic number Z. For this reason the image is referred to as a Z-contrast image. The detector performs the same

function as Lord Rayleigh's condenser lens in breaking the coherence of the imaging process. Because its angular range is much *larger* than typical Bragg angles, the coherence length in the plane of the specimen becomes much *shorter* than typical interplanar spacings. Coherence is broken between neighboring columns, and for a sufficiently small probe, they are effectively illuminated one by one as the probe scans. But the high scattering angles also ensure that the coherence is broken through the *thickness* of the sample³. At high angles coherent Bragg scattering is replaced by thermal diffuse scattering. Instead of the thickness oscillations characteristic of coherent imaging, we effectively integrate over the sample thickness, reducing dynamical oscillations to a second order effect, as shown in Fig. 2. The thickness dependence of the image becomes relatively intuitive, and saturates at an intensity again proportional to Z^2 .⁴ In the absence of strain effects, atomic images from thicker materials can therefore be interpreted equally well on the basis of simple Z-contrast.

FIG. 2. Schematic showing a fine probe formed by the objective lens of a STEM. A Z-contrast image results from mapping high angle scattered electrons as the probe is scanned across the sample. The Z-contrast image of GaAs shows As columns with higher intensity than Ga. Atomic resolution electron energy loss spectroscopy is possible with the probe stationary on specific columns selected from the image.

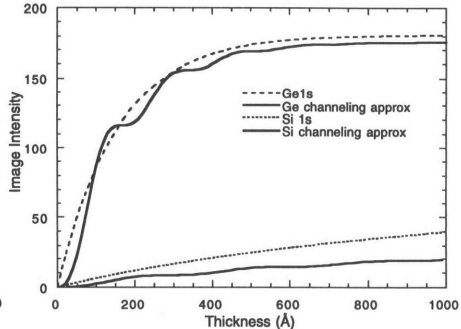
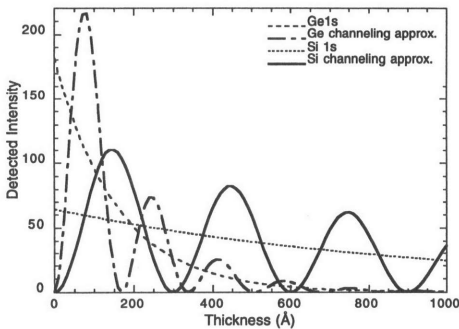
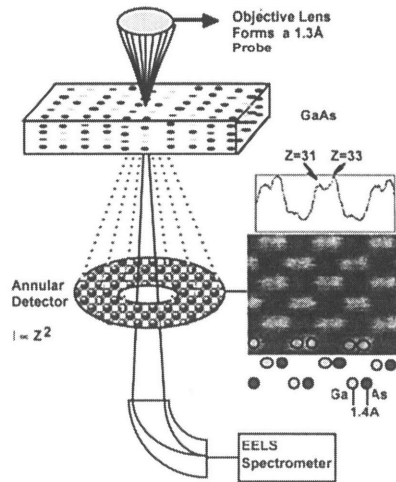


FIG. 2. Intensity of coherent scattering (left) and incoherent diffuse scattering (right) falling on a high angle annular detector as a function of specimen thickness. The diffuse scattering is the integral of the coherent scattering and dominates at sufficiently high detector angle. See ref. [2].

In the image of GaAs shown in Fig. 1, the bright features therefore correspond directly to columns of As, and the less bright features to columns of Ga. The intensity ratio is close to the expected $(33/31)^2 = 0.13$. Apart from this Z-contrast, incoherent images have no phase problem and can be directly inverted to the object using maximum entropy⁵ or similar Bayesian techniques⁶. In fact, the positions of image maxima correlate closely with the atomic column positions even close to the resolution limit, so that approximate image inversion can be carried out simply by eye. Incoherent imaging avoids the need for extensive image simulations of model structures, a particular advantage for complex materials. The VG Microscopes HB603U STEM at ORNL has a 300 kV accelerating voltage, and a directly interpretable resolution of 1.26 Å. Recently, information transfer at 0.78 Å has been demonstrated in Si<110>⁷, which demonstrates the factor of two improved resolution available with incoherent imaging; the comparable phase contrast image resolution on this microscope is 1.9 Å. There are now many examples where the high resolution and the direct interpretability of Z-contrast imaging has proved very successful. Examples include the direct determination of dislocation core structures in GaN⁸ and at CdTe/GaAs interfaces⁹, and in imaging structure and impurity sites at grain boundaries¹⁰, as shown in the examples below.

The ability to retrieve atomic structures directly from experiment is a great advantage for first principles simulations, as it avoids the need to calculate large numbers of trial structures. This is especially true for complex materials where there are a great many possibilities. A further advantage of the STEM is that it allows electron energy loss spectroscopy (EELS) to be performed simultaneously with the Z-contrast image, allowing compositional analysis and local band structure to be determined at atomic resolution¹¹. Figure 3 shows an image of a Mn-doped SrTiO₃ grain boundary with spectra obtained from selected single atomic columns. Not only is the Mn concentration determined column-by-column, but the Mn L_{2,3} fine structure suggests that the Mn valence changes from 4+ in the bulk to 3+ at the boundary.

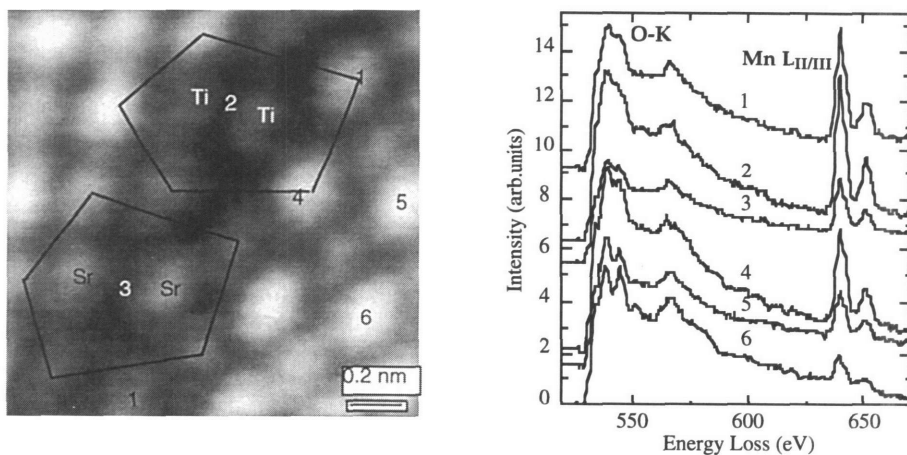


FIG. 3. Z-contrast image of a SrTiO₃ grain boundary and EELS spectra from numbered atomic columns. Mn prefers to segregate at the Ti core in the grain boundary, and changes valence from 4+ to 3+.

ORDERING IN SEMICONDUCTOR ALLOYS

Various III/V semiconductor alloys of the form $A_{1-x}B_xC$, with x near 0.5, spontaneously form ordered alloys based on the Cu-Pt structure when grown by metal-organic vapor-phase epitaxy on [001] substrates¹². Compared to the disordered alloy, these ordered structures show significant changes in optical properties including band gap reduction, valence-band splitting and polarization, and are therefore of interest for optoelectronic and solar cell applications¹³. For a small substrate miscut, domains form predominantly along only one of the four possible $\langle 111 \rangle$ directions, while for substrates close to [001] two variants are observed. Study of the distribution and nature of the ordering is of interest for understanding its origin and for controlling the domain size and distribution. Domains are conventionally imaged through dark-field diffraction contrast imaging using a superlattice spot, but this has limited resolution and only one domain can be imaged in a single exposure. Z-contrast imaging is able to reveal the compositional modulation at atomic resolution, as seen in Fig. 4 in the case of a single variant $Ga_{1-x}In_xAs$ alloy. Alternate (111) planes are seen bright over the entire field of view, and the Fourier transform of the image intensity shows the expected half-period spots. Faint half-period spots are also seen for the (11-1) variant, and examination of the image at high magnification shows short segments of this variant (Fig. 5).

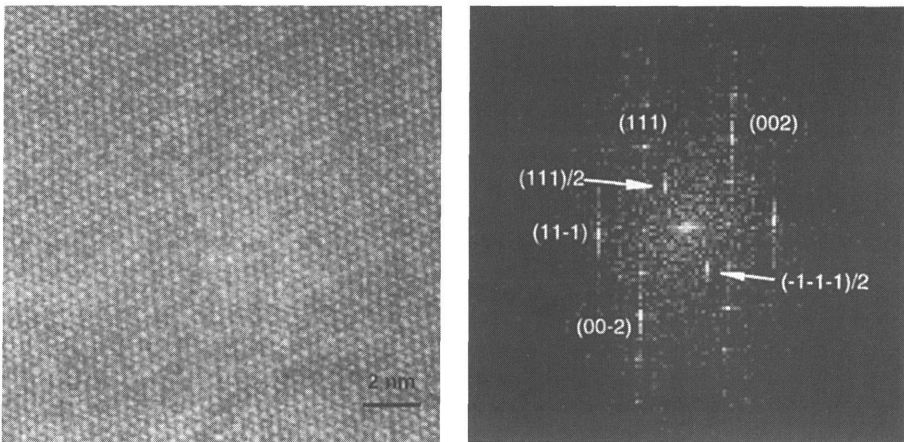
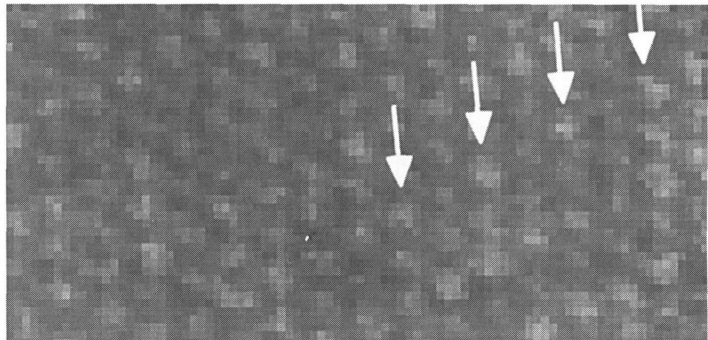


FIG. 4. Z-contrast image of a long-range single variant ordered domain in a $Ga_{1-x}In_xAs$ alloy. Clearly resolving the In concentration modulation.

FIG. 5. Enlargement of a portion of Fig. 4 showing weak ordering on the (11-1) plane.



ORDERING IN FERROELECTRIC PEROVSKITES

The nature of the ordered structure of the lead-based relaxor ferroelectric $\text{Pb}(\text{Mg}_{1/3}\text{Nb}_{2/3})\text{O}_3$ (PMN) has been the subject of controversy. Two models have been proposed for the ordering, the space-charge model¹⁴ and the charge-balanced random-layer model¹⁵. These models differ in the distribution of the B-site cations in the doubled unit cell. In the space-charge model, the B^{I} and B^{II} sites are occupied exclusively by the Mg^{2+} and Nb^{5+} cations, respectively, in the form $\text{Pb}(\text{Mg}_{1/2}\text{Nb}_{1/2})\text{O}_3$. The resulting net negative charge is assumed compensated by a disordered, Nb^{5+} rich matrix. In the charge-balanced random-layer model, microscopic charge balance is achieved by occupying the B^{II} columns exclusively by Nb^{5+} and the B^{I} columns with a random distribution of Mg^{2+} and Nb^{5+} in a 2:1 ratio. Z-contrast imaging along the [110] zone axis can easily distinguish these two cases. In the space charge structure, the ratio of B^{I} column (Mg) to B^{II} column (Nb) intensities is given by approximately 1/17, whereas, in the charge-balanced random-layer structure it is close to 1/4.

Figure 6a shows a Z-contrast image of 25% La-doped PMN [10]. The La doping increases the grain size significantly, ensuring that a single domain exists throughout the thickness of the region imaged. The intensity trace taken through the B sublattice clearly shows the intensity ratio is consistent with the 1/4 value expected for the charge-balanced random-layer model. For comparison, Fig 6b shows an image and line trace from $\text{Ba}(\text{Mg}_{1/3}\text{Nb}_{2/3})\text{O}_3$ in which the B sites are fully occupied by either Mg or Nb in a 2:1 ratio. The line trace shows the expected very weak intensity from the Mg column. A somewhat higher intensity is observed from the Mg site on the left hand side, indicating that the ordering is not entirely complete. Images were also taken from thin, undoped PMN. Although the contrast was often reduced due to the overlap of small domains through the sample thickness, the maximum value seen was still 1/4. This indicates that the ordered structure of undoped PMN also follows the charge-balanced random-layer model.

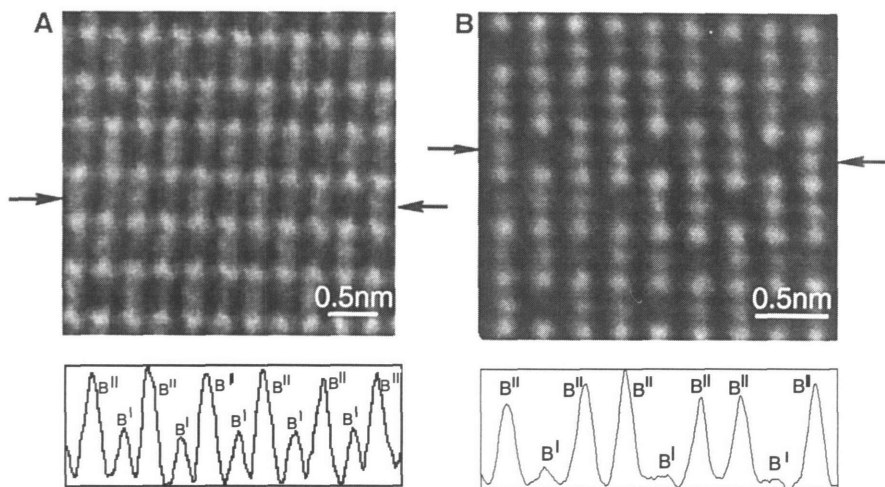


FIG. 6. Z-contrast images of (a) 25% La-doped $\text{Pb}(\text{Mg}_{1/3}\text{Nb}_{2/3})\text{O}_3$, (b) $\text{Ba}(\text{Mg}_{1/3}\text{Nb}_{2/3})\text{O}_3$ with intensity profiles across the B sublattice showing the PMN to have the charge-balanced random layer structure.

GRAIN BOUNDARY SEGREGATION SITES AND CONFIGURATIONS

Z-contrast imaging enables low concentrations of high-Z impurities to be directly observed. A recent example of this capability is shown in Fig. 7, a Z-contrast image from a 23° grain boundary in Si, after doping with As¹⁰.

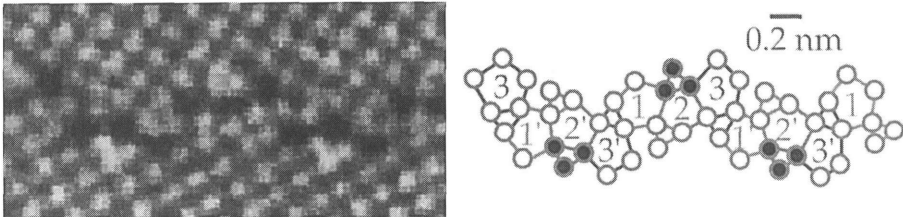


FIG. 7. Z-contrast image of a 23° $\langle 001 \rangle$ tilt grain boundary in Si showing its unexpectedly complex structure. The five-fold rings (with black centers in the image) are dislocation cores arranged in a repeating sequence along the boundary. Columns shown black in the schematic are those seen brighter in the image due to segregated As.

The atomic structure of the boundary is directly determined from the positions of the bright features in the image, and is different from all structures proposed previously. It comprises a continuous sequence of dislocation cores, a perfect edge dislocation (1) and two perfect mixed dislocations (2,3) arranged as a dipole, followed by the same sequence (1',2',3') mirrored across the boundary plane. In the $\langle 001 \rangle$ projection, these dislocations appear as a connected array of pentagonal and triangular arrangements of atomic columns. The presence of the dipoles is surprising, as being of equal and opposite Burgers vector they could equally well be replaced by perfect crystal. However, precisely the same atomic arrangement is seen in the undoped boundary given the same annealing treatment.

Looking closely at the relative intensities of the columns in the doped sample, it is seen that one of the dislocation cores contains columns that are 20% brighter on average than other similar columns. This must be due to the presence of the As dopant. Taking into account the scattering cross section, the increased intensity corresponds to an average of only 5% As concentration, approximately two As atoms in each atomic column.

In a previous theoretical study of the shorter-period 36° grain boundary, it was found that isolated As atoms have only a small segregation energy of ~ 0.1 eV, too small to account for the concentrations observed experimentally¹⁶. However, as arsenic prefers to be three-fold coordinated, calculations were performed for arsenic dimers. It was found that the two As atoms repel and become three-fold coordinated without having to create a Si dangling bond. Thus binding of the dimer occurs through repulsion. After the image of Fig. 6 was obtained, calculations were repeated for the 23° boundary, and preference was found for those sites seen bright in the image. The segregation energy was again increased, becoming consistent with the As solubility limit in the bulk at the annealing temperature of 700°C . This combined use of experimental and theoretical techniques produced a remarkably detailed and consistent atomic-scale picture of impurity segregation at this grain boundary.

Very recently, an extensive ab-initio study has confirmed the observed grain boundary structure, with its redundant dislocations, to be energetically preferred in the undoped grain boundary¹⁷. Further theoretical work could build on these results to determine grain boundary diffusion coefficients, as well as to extend studies to other boundaries and polycrystalline materials.

FUTURE DIRECTIONS

The feasibility of correcting the inherently large spherical aberration of microscope objective lenses promises to revolutionize the field of microscopy and microanalysis¹⁸¹⁹. The potential benefits for the STEM, however, may turn out to be much greater than those for the conventional TEM because it is very much less sensitive to instabilities⁷. An example of the predicted improvement in probe profile is seen in Fig. 8. The full width half maximum of the probe intensity profile decreases from 1.2 Å today to only 0.5 Å. Not only will this result in vastly greater image contrast, but the peak probe intensity increases over six-fold, so that the image signal to noise ratio will also be dramatically improved.

Figure 9 shows a simulated image of the SrTiO₃ grain boundary of Fig. 3. The Sr and Ti columns are now seen with 100% contrast, which allows the much more weakly scattering oxygen columns to just be seen. Note that the expected noise level has been added to the simulation. Interestingly, the resolution of the image is no longer limited by the incident probe, but by the channeling of the probe along the crystal columns in 1s Bloch states. These are typically ~ 0.8 Å in width, and will become the limiting resolution in a zone axis crystal.

Spectacular improvement will also be seen for EELS. Increasing the current down one selected column, and simultaneously decreasing the current illuminating surrounding columns, will improve the analytical sensitivity dramatically. Single impurity atom detection should be possible in specific columns at a grain boundary or dislocation core, with measurement of local electronic structure. Indeed, we appear to be on the threshold of finally being able to probe the atomic origins of materials properties.

FIG. 9. Simulated image of the SrTiO₃ grain boundary of Fig. 3 with the 0.5 Å probe predicted for the VG Microscopes HB603U after correction of spherical aberration.

ACKNOWLEDGMENTS

The authors are grateful to G. Duscher, and V. P. Dravid for the image in Fig. 3, and O. Krivanek for the profiles in Fig. 8. This research was supported by U.S. Department of Energy under Contract Nos. DE-AC05-96OR22464 and DE-AC36-98GO10337, and by

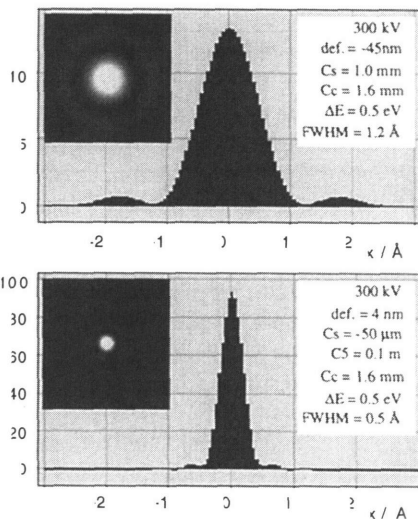
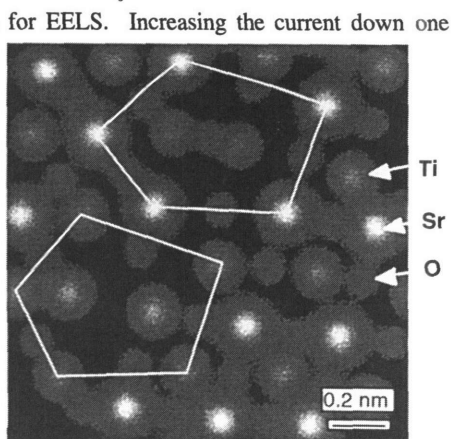


FIG. 8. Improvement in probe profile anticipated for the HB603U STEM by correction of spherical aberration. Upper panel shows probe profile and image for our present system, lower panel shows the effect of C_s correction.



appointment to the ORNL Postdoctoral Research Program administered jointly by ORNL and ORISE.

REFERENCES

- ¹, Lord Rayleigh, *Phil. Mag.* (5) **42**, 167 (1896).
- ² S. J. Pennycook, in: *Impact of Electron and Scanning Probe Microscopy on Materials Research*, edited by D. G. Rickerby, U. Valdré and G. Valdré (Kluwer Academic Publishers, The Netherlands, 1999), p. 161.
S. J. Pennycook and D. E. Jesson, *Phys. Rev. Lett.* **64**, 938 (1990).
S. J. Pennycook and D. E. Jesson, *Ultramicroscopy* **37** 14 (1991).
S. J. Pennycook and D. E. Jesson, *Acta. Metall. Mater.* **40**, S149 (1992).
R. F. Loane, P. Xu and J. Silcox, *Ultramicroscopy* **40** 121 (1992).
- ³ D. E. Jesson and S. J. Pennycook, *Proc. Roy. Soc.* **A441**, 261 (1993).
D. E. Jesson and S. J. Pennycook, *Proc. Roy. Soc. A* **449** (1995) 273.
- ⁴ P. D. Nellist and S. J. Pennycook, *Ultramicroscopy* **78** 111 (1999).
- ⁵ S. F. Gull and J. Skilling, *Maximum entropy methods in image processing*, *IEE Proc.* **131F**, 646 (1984).
- ⁶ R.C. Puetter, *International Journal of Imaging Systems and Technology* **6**, **314** (1995).
- ⁷ P. D. Nellist and S. J. Pennycook, *Phys. Rev. Lett.* **81**, 4156 (1998).
- ⁸ Y. Xin, S. J. Pennycook, N. D. Browning, P. D. Nellist, S. Sivananthan, F. Omnès, B. Beaumont, J.-P. Faurie, and P. Gibart, *Appl. Phys. Lett.* **72**, 2680 (1998).
- ⁹ A. J. McGibbon, S. J. Pennycook, and J. E. Angelo, *Science* **269**, 519 (1995).
- ¹⁰ M. F. Chisholm, A. Maiti, S. J. Pennycook, and S. T. Pantelides, *Phys. Rev. Lett.* **81**, 132 (1998).
Y. Yan, M. F. Chisholm, G. Duscher, A. Maiti, S. J. Pennycook, and S. T. Pantelides, *Phys. Rev. Lett.* **81**, 3675 (1998).
- ¹¹ N. D. Browning, M. F. Chisholm, and S. J. Pennycook, *Nature* **366**, 143 (1993).
G. Duscher, N. D. Browning, and S. J. Pennycook, *Phys. Stat. Sol. (a)* **166**, 327 (1998).
B. Rafferty and S. J. Pennycook, *Ultramicroscopy*, **78**, 141 (1999).
- ¹² E. Morita, M. Ikeda, O. Kumagai and K. Kaneko, *Appl. Phys. Lett.* **53**, 373 (1991).
C. S. Baxter and W. M. Stobbs, *Phil. Mag. A*, **69**, 615 (1994).
- ¹³ Y. Zhang and A. Mascarenhas, *Phys. Rev. B* **55**, 13100 (1997).
- ¹⁴ J. Chen, H.M. Chan and M.P. Harmer, *J. Am. Ceram. Soc.* **72**, 593 (1989).
- ¹⁵ C. Randall and A. Bhalla, *Jpn. J. Appl. Phys., Part 1* **29**, 327 (1990).
- ¹⁶ A. Maiti, M. F. Chisholm, S. J. Pennycook, and S. T. Pantelides, *Phys. Rev. Lett.* **77**, 1306 (1996).
- ¹⁷ J. R. Morris, Z.-Y Lu, D. M. Ring, J. B. Xiang, K. M. Ho, C. Z. Wang and C. L. Fu, *Phys. Rev.* **B77**, 11241 (1998).
- ¹⁸ M. Haider, S. Uhlemann, E. Schwan, H. Rose, B. Kabius and K Urban, *Nature* **392**, 768 (1998).
- ¹⁹ O. L. Krivanek, N. Delby and A. Lupini, *Ultramicroscopy*, **78**, 1 (1999).